Materials Horizons

Accepted Manuscript

This article can be cited before page numbers have been issued, to do this please use: A. Saha, Y. Li, C. Cai, L. Shi and J. Goldberger, *Mater. Horiz.*, 2026, DOI: 10.1039/D6MH00642F.

ROYAL SOCIETY OF CHEMISTRY

rsc.li/materials-horizons

View Article Online
DOI: 10.1039/D6MH00642F

New Concepts

This work introduces the concept that electronic phase transitions with large hysteresis can be exploited to decouple the triggers for high- and low-thermal-conductivity states, enabling active thermal switching far beyond the narrow windows of conventional materials. Most phase transition materials that have been targeted for thermal switching have limited thermal hysteresis and can only be switched between their high and low states within a very narrow temperature range near their phase transition. $Sm_{1-x}Gd_xS$ demonstrates that a pressure-induced, isostructural metal-insulator transition can stabilize a metastable metallic phase with a 2-fold enhancement in thermal conductivity at ambient conditions, while heating to 573 K returns the system back to its low thermal conductivity, insulating state. Both the high and low thermal conductivity state materials can be accessed across a remarkably broad 350 °C temperature window. This dual-stimulus, hysteresis-enabled mechanism establishes a new design strategy for achieving fast, reversible thermal conductivity control across extensive temperature ranges.

View Article Online
DOI: 10.1039/D6MH00642F

Data Availability

The raw data supporting this study's findings are available from the corresponding author upon reasonable request. All data supporting this work are present in the article and the Supplementary Information. The Supplemental Information includes specific heat measurements, laser flash analysis of SmS and GdS, XRD and images of pellets, Raman spectroscopy, and additional thermal conductivity analysis of $Sm_{1-x}Gd_xS$ alloys. The supplemental video shows real time conversion of gold $Sm_{0.12}Gd_{0.88}S$ pellet to the black phase upon placing the pellet on a 350 ^oC hot plate (file type, mp4).

Materials Horizons COMMUNICATION

View Article Online
DOI: 10.1039/D6MH00642F

Thermal Conductivity Switching in $Sm_{1-x}Gd_xS$ over a Broad Temperature Window via a Pressure-induced, Thermally Revertible Hysteretic Phase Transition

Ankita Saha, [a] Yudan Li [b], Chuting Cai [c], Li Shi [b c], and Joshua E. Goldberger*[a]

Received 00th January 20xx,
Accepted 00th January 20xx

DOI: 10.1039/x0xx00000x

Solid-state materials with actively tunable thermal conductivities can enable next-generation thermal management technologies. There is a need for materials that can be switched between high and low thermal conductivities over a large temperature window using different on and off triggers. Here, we establish that $Sm_{1-x}Gd_xS$ alloys, which undergo a pressure-induced, hysteretic, rock salt-to-rock salt metal-insulator transition, can be repeatedly cycled between high and low thermal conductivity states from 200 to 550 K due to differences in electronic contributions to thermal conductivity. Intermediate stoichiometries ($0.08 \leq x \leq 0.14$) transform from a mixed black/gold phase at ambient pressure to a metallic gold phase upon uniaxial compression at 1 GPa, leading to a 2-fold increase in thermal conductivity. The gold phase rapidly reverts to the equilibrium low thermal conductivity phase upon exposure to temperatures above 573 K. These findings establish that $Sm_{1-x}Gd_xS$ alloys hold promise for thermal switching and management applications.

Introduction

There has been a growing interest in enabling reversible and active control of thermal conductivity by external stimuli[1-5] for real time regulation of heat transport. Materials that are able to toggle their thermal conductivities (κ) between high (κ_{high}) and low (κ_{low}) states reversibly and on-demand may enhance system efficiency for applications such as smart buildings,[6-8] space stations,[9] and magneto/electrocaloric cooling or heating.[10, 11] Different strategies to tune the thermal conductivity rely on dynamically changing the electronic contribution (κ_{elec}) or the lattice contribution (κ_{lat}) to κ. The effectiveness of a thermal switch material is commonly evaluated by the thermal switching ratio ($\kappa_{high}/\kappa_{low}$), defined as the ratio between the maximum and minimum thermal conductivity achievable in the switching cycle.

Achieving dynamic, reversible control over thermal conductivity remains a fundamental challenge. In contrast to electronic systems where charge carriers can be modulated via electric or magnetic fields, the inherently weak coupling between external stimuli and phonons make it difficult to switch κ_{lat} dynamically. A wide array of external stimuli to trigger thermal switching has been explored including electric fields,[12, 13] magnetic fields,[14, 15] electrochemical intercalation,[16-20] mechanical strain or structural deformation,[21-24] and temperature induced phase transitions.[25-30] Very few materials have exhibited a thermal switch ratio larger than 2 over a large temperature window from 200 to 500 K.

Phase change materials, which include materials that undergo structural transitions as well as those that experience metal-insulator transitions, have the potential for enabling dynamic control of the thermal conductivity over a broad temperature range. An ideal metal-insulator transition material would have a low κ_{lat} leading to a low thermal conductivity in its insulating state, and a high thermal conductivity in its metallic state due to the additional κ_{elec}. Such an ideal material would be actively switched between the two states over a broad temperature window using triggers other than temperature. To achieve active switching, there must be sufficient hysteretic behaviour across the transition to stabilize either phase at temperatures far from the nominal metal-insulator transition temperature. Most known metal-insulator transition materials lack sufficient thermal hysteresis to enable switching between the insulating and metallic state outside a 20K temperature window.[31] For instance, VO_2 undergoes a first-order transition from an insulating monoclinic phase to a metallic rutile phase, enabling a thermal switching ratio of up to a factor of 1.5 from 3.6 to 5.4 W m^{-1} K^{-1}, due to differences in κ_{lat}. This modulation appears within a narrow 15K temperature window around 340 K, where either phase could exist.[20, 25, 27, 32].

A few other phase change materials can stabilize over a broad temperature range. The canonical phase change memory material

[a] Department of Chemistry and Biochemistry, The Ohio State University, Columbus, OH, USA
[b] Walker Department of Mechanical Engineering, The University of Texas at Austin, Austin, Texas 78712, USA
[c] Materials Science and Engineering Program, The University of Texas at Austin, Austin, Texas 78712, USA

† Footnotes relating to the title and/or authors should appear here.
Supplementary Information available: [details of any supplementary information available should be included here]. See DOI: 10.1039/x0xx00000x

View Article Online
DOI: 10.1039/D6MH00643F

$Ge_2Sb_2Te_5$ can have a large variation in its thermal conductivity that becomes 0.19 W m^{-1} K^{-1} in the amorphous state, 0.57 W m^{-1} K^{-1} in the cubic structure, and 1.57 W m^{-1} K^{-1} in the metallic hexagonal crystalline phase, due to differences in κ_{lat}.[29] All three phases can be stabilized below 420 K and can be accessed through controlled melting and cooling. Another phase change material $(Pb_{1-x}Sn_x)Se$ exhibits a reversible, temperature-controlled three-dimensional (3D)-to-two-dimensional (2D) rock salt-to-distorted rock salt phase transition, in which either phase can be accessed at temperatures from 100 to 623 K, by heating and cooling. This structural transformation enables a thermal switching ratio of 3.6 (from 0.29 to 1.1 W m^{-1} K^{-1} at 373 K) that is entirely due to κ_{lat}, by cycling the temperature across the nonequilibrium phases via actively heating above 623 K and cooling below 100 K.[33]

In comparison, $Sm_{1-x}Gd_xS$ is a distinct type of phase change material with different triggers for cycling between the high and low thermal conductivity states. SmS undergoes a pressure-induced, isostructural, first-order metal-insulator transition between a black insulating phase at ambient pressure to a gold metallic phase at approximately 6.5 kbar (Fig. 1a).[34] Both phases have a rock salt crystal structure. The unit cell volume is decreased by 15% upon the transition from the low-pressure to the high-pressure phase. The metal-insulator transition is driven by the changes in the electron configuration of Sm^{2+}. In the black insulating phase, Sm^{2+} has a localized $4f^6$ electron configuration, whereas at high pressure, Sm^{2+} is in a $4f^55d^1$ configuration in which the $5d^1$ electron is delocalized in the conduction band, giving rise to the gold, metallic phase (Fig. 1b).[35, 36] The gold SmS phase is not stable at ambient pressure and reverts to the black phase as the pressure is reduced below 1 kbar, indicating a large 5.5 kbar pressure hysteresis between the gold and black states.[37] Substituting Sm with increasing amounts of Gd reduces the transition pressure via doping and chemical pressure, until only the gold phase is stable for $Sm_{1-x}Gd_xS$ with $x \cong 0.15$.[35] Therefore, there exists a range of stoichiometries for $Sm_{1-x}Gd_xS$ ($x<0.15$) in which the thermodynamically stable black phase can be triggered to the gold phase with high pressure, stabilized at room pressure due to the large hysteresis, and can be converted back to the stable black phase at high temperature. While the thermal conductivity of the SmS black phase has been studied[38], the thermal properties of the high-pressure gold phase and the $Sm_{1-x}Gd_xS$ alloy series are unknown.

In this work, we establish the thermal conductivity differences and switching performance of $Sm_{1-x}Gd_xS$ materials. We synthesized polycrystalline $Sm_{1-x}Gd_xS$ alloys ($0.08 \leq x \leq 0.30$) along with the end members SmS and GdS. Measurements of the electrical and thermal conductivities reveal that the differences in κ are primarily driven by κ_{elec} and are increased by a factor of 3.7 from black SmS to gold GdS at room temperature. Samples having a $Sm_{1-x}Gd_xS$ stoichiometry of $0.08 \leq x \leq 0.14$, can be actively converted from a black/gold phase mixture to a phase-pure gold phase via uniaxial pressure with a concomitant 1.8-2.0× increase in total thermal conductivity. The gold phase can then be converted back to the equilibrium black/gold phase mixture upon heating to 573 K. These materials can be repeatedly cycled between the high and low κ states. The speed of conversion between the black and gold phases can occur within seconds of the application of pressure or heat triggers. Together, these results experimentally establish that a metal-insulator phase change material can be designed with a sufficiently broad hysteretic temperature window to access high and low κ states using different on and off triggers.

Materials and Methods

Synthesis

Samples of $Sm_{1-x}Gd_xS$ ($0.0 \leq x \leq 0.3$) were synthesized using a multistep process. First, SmS and GdS were synthesized by first grinding and pelletizing stoichiometric quantities of Sm, Gd, and S powders in an Ar-filled glove box, then sealing into a quartz tube and annealed at 600 °C for 24 hours followed by 1000 °C for 6 hours. Subsequently, the pellets were ground, re-pelletized, sealed in Ar-filled tantalum tubes, and then annealed at 1600 °C for 24 hours. With phase pure SmS and GdS in hand, $Sm_{1-x}Gd_xS$ ($0.0 \leq x \leq 0.3$) was synthesized by weighing out stoichiometric quantities of SmS and GdS, grinding and pelletizing, sealing in Ar-filled tantalum tubes, and annealing at 1600 °C for 24 hours.

XRD, XRF, and Specific Heat Characterization

Powder X-ray diffraction data were acquired using a Bruker D8 diffractometer configured in Bragg-Brentano geometry and equipped with Cu $K\alpha_1$ radiation. Measurements were performed over a 2θ range of 10°-80° using a sealed copper X-ray source operated at 40 kV and 40 mA. The resulting diffraction patterns were analysed and structurally refined via the Rietveld method using the GSAS-II software package.[39]

X-ray fluorescence (XRF) spectroscopy was used to determine Sm: Gd molar ratios in $Sm_{1-x}Gd_xS$ samples by using Sm_2O_3/Gd_2O_3 reference standards. XRF spectra were collected with an ARL QUANT'X energy-dispersive XRF spectrometer operated at an excitation voltage of 17 kV over an energy window spanning 0-40 keV.

Specific heat measurements of SmS were performed between 80 and 300 K using a Quantum Design 14 T PPMS DynaCool system employing the thermal relaxation technique. Milligram-scale bulk samples were mounted on a heat-capacity puck with Apiezon H grease to ensure efficient thermal contact. An additional measurement was conducted separately with just the grease to subtract from the total heat capacity. Measurements were conducted in a zero magnetic field.

In conjunction with the Laser Flash Analysis (LFA) experiments, the specific heat of SmS and GdS was measured from 300 to 400 K using a Netzsch DSC 214 Polyma differential scanning calorimetry (DSC). Pellet samples were placed in the standard Pt-Rh crucible. A sapphire sample in the standard crucible was used as a reference. An empty crucible was used as the baseline. DSC monitored the difference in the amount of heat flow required to raise the temperature of the sample and the reference at the same heating rate. The specific heat was calculated from the ratio in the measurement signals between the sample and reference upon baseline correction. In each measurement, the heating-cooling cycle was repeated three times

to stabilize the thermal history. The result for the last run was reported.

Raman Measurement

Raman scattering spectra were acquired on powders at room temperature using a Renishaw Raman IR microprobe with an inVia confocal Raman microscope, using a 514 nm laser, and a charge-coupled detector. The 50 mW laser power, 1800 lines/mm grating size, and acquisition times were kept the same for all samples. Eight random spots of each sample were measured to confirm the uniformity of the spectrum.

Steady State Electronic and Thermal Conductivity Measurements

Electronic conductivity and thermal conductivity measurements from 80 to 400 K were conducted with the samples in a Janis SuperTran cryostat system (Lakeshore) with liquid nitrogen as the cryogen. Electronic conductivity measurements were performed using the 4-probe method, and thermal conductivity measurements were collected using the steady-state method with the sample joined in series with a heater and a heat sink. A typical measurement setup is shown in Figure S1. Highly thermally and electrically conductive silver-based epoxy (EPO-TEK H20E) was used to affix brass sheets on the top and bottom surfaces of the sample. The sheets serve as current spreaders to provide a uniform electrical and thermal current flow. The sample was then mounted onto an insulating alumina baseplate, which acted as the mounting plate and heat sink, assuring uniform heat flow in the samples. Current wires (20 μm copper wire) were affixed to the top and bottom brass plates. Type-T thermocouples comprised of the same 20 μm copper wire and Constantan wire that were placed 2-3 mm apart along the pellet length. Finally, a resistive heater was affixed to the top surface for thermal conductivity measurements. For electrical conductivity measurements, the 20 μm copper wires were used as the measurement leads. The samples were then placed in a vacuum environment inside the cryostat. The temperature was allowed to stabilize for at least one hour before each measurement.

For thermal conductivity measurements, heat was applied to the sample through a resistive heater until a steady-state temperature gradient >3 K was established. The power to the resistive heater was held constant for approximately 5 minutes to ensure thermal equilibrium, prior to recording the thermal conductivity.

The total thermal conductivity $\boldsymbol{\kappa}$ is obtained via the equation.

$$\kappa = \frac{Q * l}{A * \Delta T}$$

In this method, Q is the heat conducted through the sample, l is the distance between the thermocouples, A is the pellet cross-sectional area, and ΔT denotes the temperature difference measured between the thermocouples. The total power generated by the heater (Q_H) was calculated from $Q_H = V_H I_H$, where V_H and I_H are the heater voltage and current, respectively. A portion of Q_H is lost to the surroundings via conduction and radiation. To suppress convective and conductive heat losses through air, measurements were conducted under vacuum conditions of approximately 10^{-4} Torr. The diameter of the lead wires is as small as 20 μm to reduce conductive loss through them. Radiative heat losses could not be fully eliminated. A calibration was carried out by repeating the measurements on an iron reference bar with a known thermal conductivity ($\boldsymbol{\kappa}_{Iron}$). The heat loss ($Q_L$) was calculated to be $Q_L = V_{HQ} I_{HQ} - \boldsymbol{\kappa}_{Iron} \Delta T_Q * A_{Iron} / L_{Iron}$ where V_{HQ} and I_{HQ} are the heater voltage and current, respectively, and A_{Iron} and L_{Iron} are the cross section and length of the iron bar. For this calibration sample, the Q_L / Q_H ratio ranges from 0.02 at 200 K to 0.29 at 400 K. Although this ratio could increase for samples with a decreased thermal conductivity and increased surface emissivity, here the measured Q_L with the iron reference is used to estimate the heat loss to determine the heat input into the sample as $Q = Q_H - Q_L$.

Near room temperature, the dominant sources of uncertainty in the thermal conductivity obtained from the static heater-sink technique arise from radiative heat losses and geometric uncertainties. The latter is usually dominated by the spacing between the thermocouples, where the error is given by the ratio between the size of the thermocouple contacts (which gives the uncertainty) and the distance between them. In this work, the resulting uncertainty is estimated to fall within the range of 8-15% (Supplementary information).

Thermal conductivity was also determined via the laser flash analysis (LFA) technique. The thermal diffusivity (α) of SmS and GdS pellets with thicknesses of 1.34 mm and 1.35 mm respectively, and diameters of 5.98 mm were measured using a Netzsch LFA 457 laser flash apparatus. In the measurements, laser shots were repeated 3 times at each temperature that was increased from 300 to 400 K and decreased back in 20 K increments. The thermal diffusivity was calculated by fitting the temperature-time signal curves based on Cape-Lehmann + pulse correction model. The thermal conductivity was calculated as $\kappa = \alpha \rho C_p$ The reported uncertainty is the standard deviation of the measurement results.

View Article Online
DOI: 10.1039/D6MH00642F

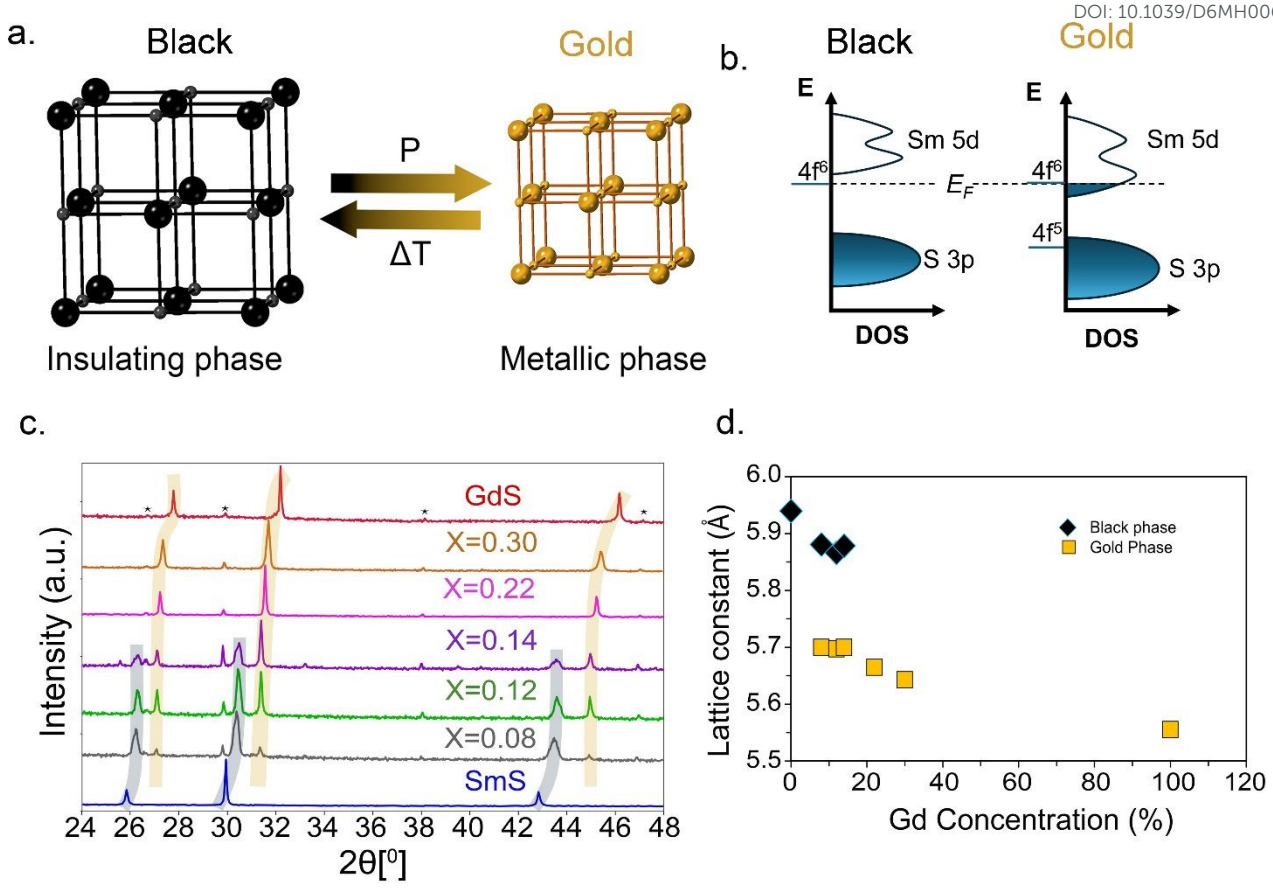

Fig. 1 Structural evolution and characterization of $Sm_{1-x}Gd_xS$ ($0 < x < 0.3$). a) Schematic illustration showing the switching from the equilibrium cubic insulating black phase to the cubic metallic gold phase with pressure and reverting to the black phase with heat. b) Simplified density of states diagram illustrating the differences between the black and gold phases. The delocalized Sm 5d and S 3p bands are on the right side of the Energy axes, and the localized Sm 4f states are depicted as lines to the left. c) XRD patterns of $Sm_{1-x}Gd_xS$ samples showing the peaks of the larger unit cell black phase (highlighted in grey), the smaller unit cell gold phase (highlighted in orange), and trace $(Sm_{1-x}Gd_x)_2O_2S$ impurities (starred). d) Lattice parameters as a function of Gd concentration of the black and gold phase, determined from Rietveld refinements.

Results and Discussion

Polycrystalline pellets of $Sm_{1-x}Gd_xS$ ($0<x<0.3$) alloy phases were prepared by first synthesizing gold GdS and black SmS and then annealing them together at 1600^0C. X-ray diffraction (XRD) and Rietveld analysis were performed to determine the ratios of the black to gold phase, the phase purities, and the lattice parameters for each alloy (Fig. 1c, d, Table 1). X-ray Fluorescence measurements confirmed the overall Sm:Gd ratio. The ratio of the black and gold phase can be determined by the composition. This decrease is consistent with previous studies on these alloys,[35] and is expected due to the smaller radius of Gd than Sm due to presence of a larger and smaller unit cell rock salt lattice, respectively. For SmS and $Sm_{0.95}Gd_{0.05}S$, only the large unit cell rock salt phase of the black phase was observed. For $Sm_{1-x}Gd_xS$ ($0.08\leq x\leq 0.14$), a mixture of both the black and gold $Sm_{1-x}Gd_xS$ phases was observed (Fig. 1c). Only the small unit cell lattice gold phase was observed for $x\geq 0.22$. In all samples, impurity $(Sm_{1-x}Gd_x)_2O_2S$ phase fractions of less than 10% were observed. SmS has a lattice constant of 5.9398(1) Å. The lattice parameter of the black phase decreases with increasing quantities of Gd. The lattice constant of the gold phase that first appears in $Sm_{0.92}Gd_{0.08}S$ is 5.6997(2) Å and decreases with increasing Gd.

Next, the thermal and electronic transport properties were obtained on the sintered as-grown pellets at temperatures from 80 to 400 K, to follow their evolution with Gd incorporation. The density of these sintered pellets ranged from 82-85% of the theoretical density for all samples. The mixed black/gold $Sm_{1-x}Gd_xS$ ($0.08\leq x\leq 0.14$) phases were not measured below 200 K, as

Materials Horizons COMMUNICATION

View Article Online
DOI: 10.1039/D6MH00642F

Table 1. Summary of stoichiometry, lattice parameters, and phase fractions for $Sm_{1-x}Gd_xS$ samples, showing contributions from black and gold phases along with $(Sm_{1-x}Gd_x)_2O_2S$ impurity.

Stoichiometry	Black a [Å]	%Black [Phase %]	Gold a [Å]	%Gold [Phase %]	$(Sm_{1-x}Gd_x)_2O_2S$ impurity [Phase %]
SmS	5.9398(1)				
$Sm_{0.92}Gd_{0.08}S$	5.8807(3)	85.5(6) %	5.6997(2)	9.5(5) %	5.0(4) %
$Sm_{0.88}Gd_{0.12}S$	5.8663(2)	61.1(5) %	5.6970(1)	31.7(4) %	7.2(5) %
$Sm_{0.86}Gd_{0.14}S$	5.8646(6)	39.7(4) %	5.6945(5)	51.5(4) %	8.8(2) %
$Sm_{0.78}Gd_{0.22}S$			5.6659(9)		3.3(3) %
$Sm_{0.70}Gd_{0.30}S$			5.6423(1)		3.9(3) %
GdS			5.5553(1)		4.0(1) %

these compounds undergo a second low-temperature phase transition that results in sample fracturing.[35] The electrical conductivities (σ) increase with Gd incorporation starting from the semiconducting black SmS phase to the mixed black/gold $Sm_{1-x}Gd_xS$ ($0.08 \leq x \leq 0.14$) phases, and to the gold $Sm_{1-x}Gd_xS$ ($x \geq 0.22$) phases (Fig. 2a). The electrical conductivity of SmS is 5.56×10^3 S m^{-1} at room temperature and increases with increasing temperature as would be expected for a semiconducting phase. In comparison, the electrical conductivities of the mixed black/gold $Sm_{1-x}Gd_xS$ ($0.08 \leq x \leq 0.14$) phases are high and range between 4.02×10^4 and 1.10×10^5 S m^{-1} at 300 K.

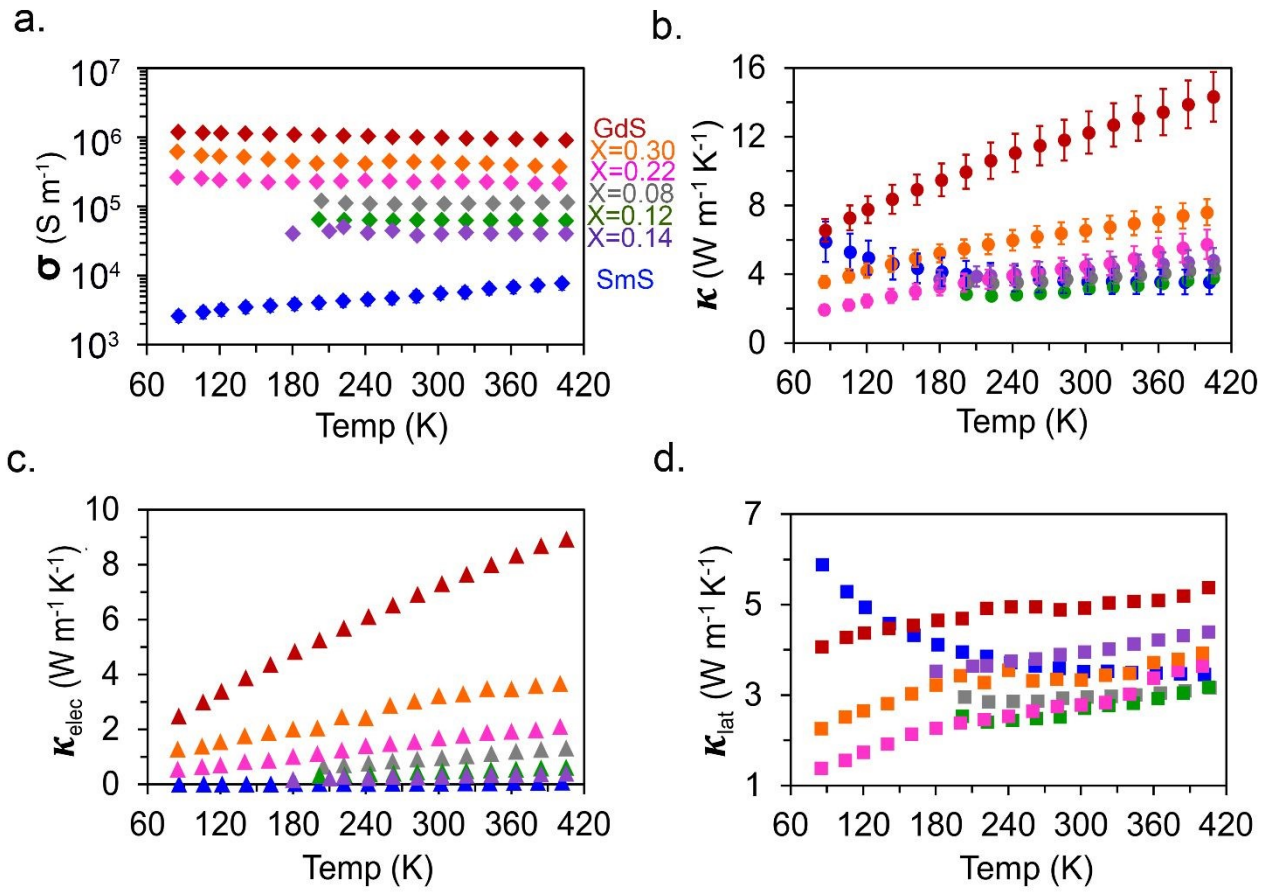

Fig. 2 Electronic and thermal conductivities of $Sm_{1-x}Gd_xS$. a) Electrical conductivity versus temperature. b) Total thermal conductivity versus temperature. c) Temperature-dependent electronic thermal conductivity estimated from the Wiedemann-Franz law. d) Temperature-dependent lattice thermal conductivity

View Article Online
DOI: 10.1039/D6MH00642F

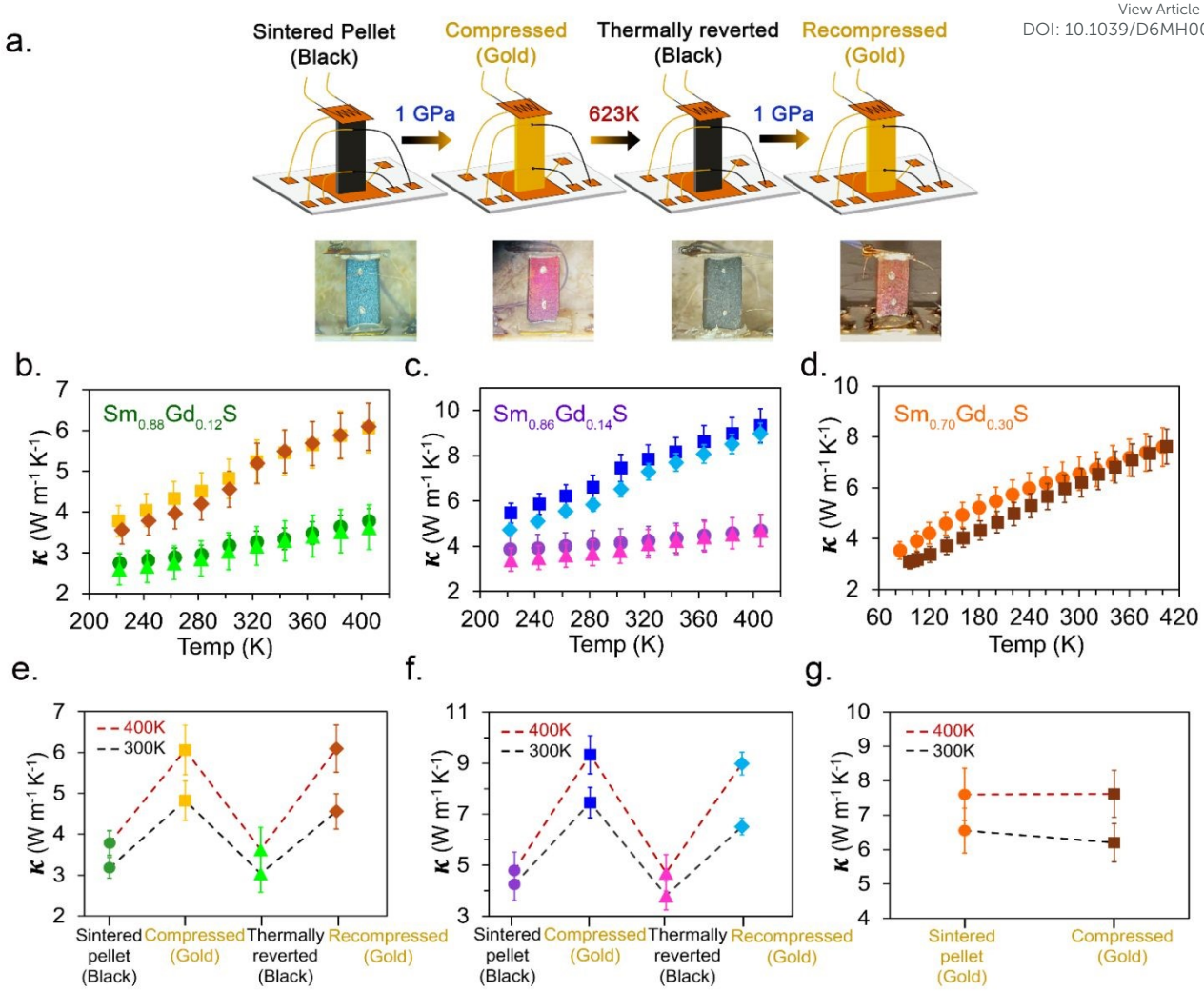

Fig. 3 Thermal conductivity under external triggers. a) Cycling of $Sm_{1-x}Gd_xS$ ($0.08 \leq x \leq 0.14$) through the metal-insulator transition by pressure (black to gold) and annealing (reversion to black phase). b-d) Thermal conductivity evolution of the as-grown sintered pellet, compressed, annealed, and re-compressed samples of $Sm_{0.88}Gd_{0.12}S$, $Sm_{0.86}Gd_{0.14}S$, and $Sm_{0.70}Gd_{0.30}S$, respectively. e-g) Thermal conductivity of the same compositions after these triggers at 300 K (black dashed line) and 400 K (red dashed line). In b and e, the dark green circles correspond to the sintered pellet-black phase, the yellow squares correspond to the compressed-gold phase, the light green triangles correspond to the thermally reverted-black phase, and the brown diamonds correspond to the recompressed-gold phase measurements. In c and f, the purple circles correspond to the sintered pellet-black phase, the blue squares correspond to the compressed-gold phase, the pink triangles correspond to the thermally reverted-black phase, and the light blue diamond shapes correspond to the recompressed-gold phase measurements. In d and g, the orange circles correspond to the sintered pellet-gold phase, the dark brown squares correspond to the compressed non-changed gold phase. For simplicity, samples with black/gold phase mixtures are labelled as "black".

Among these three samples, the electrical conductivities decrease with increasing fraction of the insulating $(Sm_{1-x}Gd_x)_2O_2S$ impurity phase. The electrical conductivities of the gold $Sm_{1-x}Gd_xS$ ($x \geq 0.22$) phases show a further increase with increasing Gd concentration. GdS has a large room temperature electrical conductivity of 1×10^6 S m^{-1}, which approaches values of elemental metals. The electrical conductivity of these gold phases decrease with increasing temperature, as would be expected for a metal.

The κ of these materials above 300 K show a similar dependence on the composition as the electrical conductivity. At 400 K, SmS has the lowest value of 3.5 W m^{-1} K^{-1}, followed by 3.8 to 4.8 W m^{-1} K^{-1} for the mixed black/gold $Sm_{1-x}Gd_xS$ ($0.08 \leq x \leq 0.14$) alloys, 5.7 to 7.6 W m^{-1} K^{-1} for the gold $Sm_{1-x}Gd_xS$ ($x=0.22$, 0.30) alloys, and 14.3 W m^{-1} K^{-1} for GdS (Fig. 2b). The thermal conductivity of the purely semiconducting SmS phase shows a characteristic 1/T dependence on temperature (T) above 80 K (Figure S2), indicating a phononic origin of the thermal conductivity, in contrast to the metallic and mixed metallic phases. The thermal conductivities of SmS and GdS were further confirmed by laser flash diffusivity measurements from 300 - 400 K, which when combined with measured specific heat values and densities for each sample, resulting in similar thermal conductivities within measurement errors (Figure S3).

The contributions of κ_{elec} and κ_{lat} to the total thermal conductivities were then extracted for each stoichiometry (Fig. 2c, d). κ_{elec} was estimated using the Wiedemann-Franz law, $\kappa_{elec} = L\sigma T$, where $L = 2.44 \times 10^{-8}$ V^2 K^{-2} is the Lorenz number, and T is the temperature. κ_{lat} was determined by subtracting κ_{elec} from κ.

The standard Lorenz number is assumed to remain valid across the measured temperature range, even with f-electrons near the frontier bands, since deviations from this value due to inelastic electron-phonon scattering and correlation effects generally occur only at low temperatures in most metallic materials.[40] Supporting a metallic instead of semiconducting behaviour where the electronic thermal conductivity measured in the close-loop condition would contain an additional σS^2T term compared to the open-loop measurement, thermopower measurements for all Gd-containing samples show that S^2/L <<0.07 across the temperature range (Figure S4). In addition, the temperature range of these measurements is much higher than the Debye temperature of SmS (155±7K),[41] supporting dominant small-angle, quasielastic electron-phonon scattering. This material system has not shown correlated electron transport behaviour at the temperature range of the measurements.

The total thermal conductivity of SmS is almost entirely due to κ_{lat}, as a consequence of low electronic conductivity in black insulating phase. The mixed black/gold $Sm_{1-x}Gd_xS$ ($0.08 \leq x \leq 0.14$) phases have electrical conductivities that are almost 1-2 orders of magnitude higher than SmS, leading to an increase in κ_{elec} of 0.4 -1 W m^{-1} K^{-1} at 400 K. The purely metallic gold phases of $Sm_{1-x}Gd_xS$ (x=0.22, 0.30) have electronic conductivities above 2×10^5 S m^{-1} at 400 K, which results in significantly enhanced κ_{elec} values of 2.1 and 3.7 W m^{-1} K^{-1}, respectively. The highly conducting GdS phase has a large κ_{elec} of 8.9 W m^{-1} K^{-1}.

Across the alloy series, κ_{lat} remains relatively similar at high temperatures (3.2 - 4.4 W m^{-1} K^{-1} at 400 K), except for GdS, which has a much higher κ_{lat} (5.4 W m^{-1} K^{-1}at 400 K), attributed to its much smaller lattice parameter (5.55 Å). Raman spectroscopy of the alloys was performed across the alloy series (Figure S5) and the spectra match those previously reported for SmS.[42] The first order optical phonon mode ranges from 185-187 cm^{-1}, across the entire series, and there is a negligible change in the full width at half maximum, which suggest that alloy or defect scattering plays a minimal role in the phonon band structure. This is likely a consequence of the fact that the natural isotopic composition of Sm and Gd contain 5 and 6 stable isotopes, respectively, reducing the alloy or defect mixing and scattering effects of lanthanide substitutions. Future confirmation of the change in the phonon modes will require investigations via inelastic neutron scattering. Taken together, this analysis shows that the changes in κ among all stoichiometries are largely due to changes in κ_{elec}, although the extracted lattice thermal conductivity also varies between different compositions (Fig. 2d).

We then evaluated the changes in thermal conductivity in the mixed stoichiometries $Sm_{1-x}Gd_xS$ ($0.08 \leq x \leq 0.14$) by cycling through the metal-insulator transition by applying uniaxial pressure to convert these phases into the gold phase and reverting to the mixed black/gold ground state by annealing (Fig. 3a, Figure S6). First, the 1600 ^{0}C "sintered" $Sm_{1-x}Gd_xS$ pellets were ground into powders and then compressed at 1 GPa using a rectangular pellet press for 60 s, causing the samples to turn copper coloured. The XRD patterns of the compressed pellets show that $Sm_{0.88}Gd_{0.12}S$ and $Sm_{0.86}Gd_{0.14}S$ are exclusively in the gold phase, whereas $Sm_{0.92}Gd_{0.08}S$ contains the residual black semiconducting phase (Figure S7). The total thermal conductivity has significantly increased for all three samples. At 400 K, κ for $Sm_{0.88}Gd_{0.12}S$ and $Sm_{0.86}Gd_{0.14}S$ increased from 3.8 to 6.1 W m^{-1} K^{-1}, and 4.7 to 9.3 W m^{-1} K^{-1}, respectively (Fig. 3b, c, e, f). Despite incomplete conversion into the gold phase, $Sm_{0.92}Gd_{0.08}S$ also exhibited an increased κ after compression from 4.3 to 5.9 W m^{-1} K^{-1} (Figure S8).

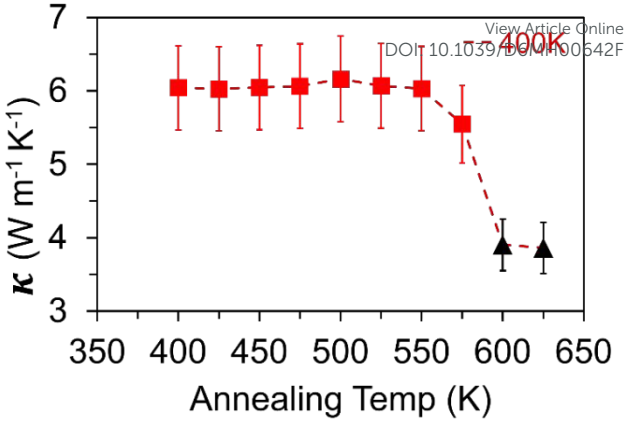

Fig. 4 The temperature at which the high κ gold $Sm_{0.88}Gd_{0.12}S$ thermally reverts to the equilibrium mixed phase. The thermal conductivity of $Sm_{0.88}Gd_{0.12}S$ was measured at 400 K after annealing for 20 minutes at each temperature, showing that $Sm_{0.88}Gd_{0.12}S$ reverts to the mixed phase above 550 K.

Next, to revert the compressed pellets to their mixed black/gold ground states, the pellets were placed on a 623 K (350^{0}C) hot plate for 15 s under an Ar atmosphere. An immediate colour change was observed upon placing them on the hot plate, and the pellets had become black within 5 s (Supplementary video). XRD analysis of these thermally reverted pellets showed that the samples had converted back to mixed black-gold phases. The thermal conductivities of these thermally reverted pellets were nearly identical to the originally measured "sintered pellet" mixed black/gold phases. To confirm the reproducibility of this thermal conductivity swing, the pellets were placed back into the rectangular press and "re-compressed" at 1 GPa for 60 s, after which the pellets converted again into the pure gold phase based on the XRD pattern (Figure S7a-c). The κ of the "recompressed" gold phases are within measurement error of the originally measured compressed gold phase. This process was repeated over 10 times on the same pellet, during which identical thermal conductivity changes between the black and gold phases were observed, within the measurement error (Figure S9).

Finally, the same compression-annealing procedure was performed on the non-switching $Sm_{0.70}Gd_{0.30}S$ stoichiometry as a negative control (Fig. 3d, g). No significant changes in κ were observed between the sintered and compressed phases of this control. XRD analysis confirms that this stoichiometry remains entirely as the gold phase even after compression at 1 GPa (Figure S7d). Furthermore, the electrical conductivity before and after compression are identical within measurement error (Figure S10), which rules out interference from additional defect scattering caused by compression, offsetting any changes caused by changes in κ_{elec} in these materials.

To determine the temperature range at which thermal switching can occur, we evaluated the temperature at which a compressed $Sm_{0.88}Gd_{0.12}S$ alloy thermally reverts to the equilibrium mixed phase. The $Sm_{0.88}Gd_{0.12}S$ device was annealed for 20 minutes over the temperature range of 400-625 K in 25 K increments. Following each annealing step, κ was measured at 400 K using the steady state approach (Fig. 4). Annealing between 400 and 550 K produces negligible changes in κ, indicating $Sm_{0.88}Gd_{0.12}S$ remains in the high κ gold state. In contrast, annealing above 550 K leads to a reduction in κ and by 600 K the system has undergone a complete reversion from the metallic gold phase to the mixed equilibrium phase. The transition temperature was observed for the $Sm_{1-x}Gd_xS$ (x=0.08, 0.14) phases. Thus, thermal switching in $Sm_{1-x}Gd_xS$ can be achieved between 200-550 K.

Several features of $Sm_{1-x}Gd_xS$ make it a unique material for thermal switching. First, in contrast to most metal-insulator transition materials that have been evaluated for thermal switching, the changes in thermal conductivity are largely due to changes in κ_{elec}. The gold phases have sufficiently high electronic conductivities to produce κ_{elec} values comparable to κ_{lat}. This is in part due to their high free carrier density of ~1 e^- per Sm or Gd atom in the compressed gold phases, as well as the highly symmetric rock salt crystal structure that produces more widely disperse bands, with effective mass values of m*=1.2.[43, 44] Second, the ability to access both the high thermal conductivity gold phase and the equilibrium low thermal conductivity mixed phase over a broad temperature range is a direct consequence of the large hysteresis of the metal-insulator transition in $Sm_{1-x}Gd_xS$, the origin of which may be similar to SmB_6.[45]

Finally, the 1 GPa pressure needed to induce the metal-insulator transition is accessible for thermal switching devices, especially if thin films of $Sm_{1-x}Gd_xS$ can be created. In a commercial device setting, single-crystal thin film form factors would potentially have faster switching kinetics and potentially an enhanced long-term structural stability upon repeated cycling, compared to the polycrystalline pellets measured here. Along these lines, SmSe thin films which undergo a type-II pressure-dependent metal-insulator transition, have been utilized as piezoresistive sensors in devices with piezoelectric actuators capable of reaching 2 GPa.[46, 47]

Conclusions

$Sm_{1-x}Gd_xS$ alloys show promising properties for thermal switching applications. In contrast to nearly all other metal-insulator transition materials, which switch between their κ_{high} and κ_{low} states at a specific temperature, the large pressure hysteresis in the $Sm_{1-x}Gd_xS$ enables different triggers for switching into the κ_{high} state with pressure and into the κ_{low} state with temperature. $Sm_{1-x}Gd_xS$ alloys can be triggered between κ_{high} and κ_{low} states with $\kappa_{high}/\kappa_{low}$ ratios up to 2, exhibit fast switching (within 5-15 seconds), and both states can be accessed over a broad 200-550 K temperature range. We established that the differences in thermal conductivity along the $Sm_{1-x}Gd_xS$ alloy series are largely due to the additional κ_{elec} contributions as the material changes from the semiconducting black phase to the metallic gold phase. These results identify $Sm_{1-x}Gd_xS$ as an emerging thermal switching active material for future thermal management technologies.

Author contributions

AS was responsible for data curation, formal analysis, investigation, and writing the original draft, review, and editing. YL was responsible for data curation, formal analysis, and investigation. CC was responsible for data curation, formal analysis, and investigation. LS was responsible for formal analysis, investigation, supervision, and editing the manuscript. JEG was responsible for conceptualization, funding acquisition, supervision, and writing the original draft, review, and editing.

Conflicts of interest

There are no conflicts to declare.

Data Availability

The raw data supporting this study's findings are available from the corresponding author upon reasonable request. All data supporting this work are present in the article and the Supplementary Information. The Supplemental Information includes specific heat measurements, laser flash analysis of SmS and GdS, XRD and images of pellets, additional thermal conductivity analysis of $Sm_{1-x}Gd_xS$ alloys. The supplemental video shows real time conversion of gold $Sm_{0.12}Gd_{0.88}S$ pellet to the black phase upon placing the pellet on a 350 ^oC hot plate (file type, mp4).

Acknowledgement

We graciously acknowledge and dedicate this work to Prof. Joseph P. Heremans for providing useful guidance and feedback. We acknowledge the U.S. Office of Naval Research MURI "Extraordinary electronic switching of thermal transport" Grant No. N00014-21-1–2377. Partial funding for shared facilities used in this research was provided by the Center for Emergent Materials: an NSF MRSEC under award number DMR-2011876.

Notes and references

(1) G. Wehmeyer, T. Yabuki, C. Monachon, J. Wu and C. Dames, Thermal diodes, regulators, and switches: Physical mechanisms and potential applications, *Appl. Phys. Rev.* 2017, **4**, 041304. DOI: 10.1063/1.5001072

(2) Y. Li, W. Li, T. Han, X. Zheng, J. Li, B. Li, S. Fan and C. W. Qiu, Transforming heat transfer with thermal metamaterials and devices,

Nat. Rev. Mater. 2021, **6**, 488–507. DOI: 10.1038/s41578-021-00283-2

(3) H. Kim, G. Park, S. Park and W. Kim, Strategies for Manipulating Phonon Transport in Solids, *ACS Nano* 2021, **15**, 2182–2196. DOI: 10.1021/acsnano.0c10411

(4) Z. Xiang, F. Zhang and B. Liao, High-Throughput Discovery of Semiconductors with Antibonding Valence Band and Bonding Conduction Band, *ACS Mater. Lett.* 2025, **7**, 3916–3921. DOI: 10.1021/acsmaterialslett.5c01111

(5) H. Babaei, K. R. Meihaus and J. R. Long, Reversible Thermal Conductivity Switching Using Flexible Metal-Organic Frameworks, *Chem Mater* 2023, **35**, 6220–6226. DOI: 10.1021/acs.chemmater.3c00496

(6) S. Lee and P. Karava, Towards smart buildings with self-tuned indoor thermal environments – A critical review, *Energy Build.* 2020, **224**, 110172. DOI: 10.1016/j.enbuild.2020.110172

(7) K. Menyhart and M. Krarti, Potential energy savings from deployment of Dynamic Insulation Materials for US residential buildings, *Build. Sci.* 2017, **114**, 203–218. DOI: 10.1016/j.buildenv.2016.12.009

(8) M. Luo, Z. Wang, K. Ke, B. Cao, Y. Zhai and X. Zhou, Human metabolic rate and thermal comfort in buildings: The problem and challenge, *Build. Sci.* 2018, **131**, 44–52. DOI: 10.1016/j.buildenv.2018.01.005

(9) D. W. Hengeveld, M. M. Mathison, J. E. Braun, E. A. Groll and A. D. Williams, Review of Modern Spacecraft Thermal Control Technologies, *HVAC&R Res.* 2011, **16**, 189–220. DOI: 10.1080/10789669.2010.10390900

(10) R. I. Epstein and K. J. Malloy, Electrocaloric devices based on thin-film heat switches, *J. Appl. Phys.* 2009, **106**, 064509. DOI: 10.1063/1.3190559

(11) K. Klinar, J. Y. Law, V. Franco, X. Moya and A. Kitanovski, Perspectives and Energy Applications of Magnetocaloric, Pyromagnetic, Electrocaloric, and Pyroelectric Materials, *Adv. Energy Mater.* 2024, **14**, 2401739. DOI: 10.1002/aenm.202401739

(12) J. F. Ihlefeld, B. M. Foley, D. A. Scrymgeour, J. R. Michael, B. B. McKenzie, D. L. Medlin, M. Wallace, S. Trolier-McKinstry and P. E. Hopkins, Room-temperature voltage tunable phonon thermal conductivity via reconfigurable interfaces in ferroelectric thin films, *Nano Lett.* 2015, **15**, 1791–1795. DOI: 10.1021/nl504505t

(13) M. Li, H. Wu, E. M. Avery, Z. Qin, D. P. Goronzy, H. D. Nguyen, T. Liu, P. S. Weiss and Y. Hu, Electrically gated molecular thermal switch, *Science* 2023, **382**, 585–589. DOI: 10.1126/science.abo4297

(14) L. Castelli, Q. Zhu, T. J. Shimokusu and G. Wehmeyer, A three-terminal magnetic thermal transistor, *Nat. Commun.* 2023, **14**, 393. DOI: 10.1038/s41467-023-36056-4

(15) K. G. Koster, J. Hise, J. P. Heremans and J. E. Goldberger, Giant Magnetothermal Conductivity Switching in Semimetallic WSi2 Single Crystals, *Adv. Electron. Mater.* 2024, **6**, 1757–1762. DOI: 10.1021/acsaelm.3c01662

(16) J. Cho, M. D. Losego, H. G. Zhang, H. Kim, J. Zuo, I. Petrov, D. G. Cahill and P. V. Braun, Electrochemically tunable thermal conductivity of lithium cobalt oxide, *Nat. Commun.* 2014, **5**, 4035. DOI: 10.1038/ncomms5035

(17) J. S. Kang, M. Ke and Y. Hu, Ionic Intercalation in Two-Dimensional van der Waals Materials: In Situ Characterization and Electrochemical Control of the Anisotropic Thermal Conductivity of Black Phosphorus, *Nano Lett.* 2017, **17**, 1431–1438. DOI: 10.1021/acs.nanolett.6b04385

(18) A. Sood, F. Xiong, S. Chen, H. Wang, D. Selli, J. Zhang, C. J. McClellan, J. Sun, D. Donadio, Y. Cui, E. Pop and K. E. Goodson, An electrochemical thermal transistor, *Nat. Commun.* 2018, **9**, 4510. DOI: 10.1038/s41467-018-06760-7

(19) A. Jeong, M. Yoshimura, H. Kong, Z. Bian, J. Tam, B. Feng, Y. Ikuhara, T. Endo, Y. Matsuo and H. Ohta, High-performance solid-state electrochemical thermal switches with earth-abundant cerium oxide, *Sci. Adv.* 2025, **11**, eads6137. DOI: 10.1126/sciadv.ads6137

(20) H. Kizuka, T. Yagi, J. Jia, Y. Yamashita, S. Nakamura, N. Taketoshi and Y. Shigesato, Temperature dependence of thermal conductivity of VO2 thin films across metal–insulator transition, *Jpn. J. Appl. Phys.* 2015, **54**, 053201. DOI: 10.7567/jjap.54.053201

(21) C. M. Hartquist, B. Li, J. H. Zhang, Z. Yu, G. Lv, J. Shin, S. V. Boriskina, G. Chen, X. Zhao and S. Lin, Reversible two-way tuning of thermal conductivity in an end-linked star-shaped thermoset, *Nat. Commun.* 2024, **15**, 5590. DOI: 10.1038/s41467-024-49354-2

(22) S. Li, Z. Qin, H. Wu, M. Li, M. Kunz, A. Alatas, A. Kavner and Y. Hu, Anomalous thermal transport under high pressure in boron arsenide, *Nature* 2022, **612**, 459–464. DOI: 10.1038/s41586-022-05381-x

(23) X. Meng, T. Pandey, J. Jeong, S. Fu, J. Yang, K. Chen, A. Singh, F. He, X. Xu, J. Zhou, W. P. Hsieh, A. K. Singh, J. F. Lin and Y. Wang, Thermal Conductivity Enhancement in MoS2 under Extreme Strain, *Phys. Rev. Lett.* 2019, **122**, 155901. DOI: 10.1103/PhysRevLett.122.155901

(24) Y. Zhou, Z. Y. Dong, W. P. Hsieh, A. F. Goncharov and X. J. Chen, Thermal conductivity of materials under pressure, *Nat. Rev. Phys.* 2022, **4**, 319–335. DOI: 10.1038/s42254-022-00423-9

(25) D. W. Oh, C. Ko, S. Ramanathan and D. G. Cahill, Thermal conductivity and dynamic heat capacity across the metal-insulator transition in thin film VO2, *Appl. Phys. Lett.* 2010, **96**, 151906. DOI: 10.1063/1.3394016

(26) R. Zheng, J. Gao, J. Wang and G. Chen, Reversible temperature regulation of electrical and thermal conductivity using liquid-solid phase transitions, *Nat. Commun.* 2011, **2**, 289. DOI: 10.1038/ncomms1288

(27) R. Xie, C. T. Bui, B. Varghese, Q. Zhang, C. H. Sow, B. Li and J. T. L. Thong, An Electrically Tuned Solid-State Thermal Memory Based on Metal–Insulator Transition of Single-Crystalline VO2 Nanobeams, *Adv. Funct. Mater.* 2011, **21**, 1602–1607. DOI: 10.1002/adfm.201002436

(28) K. Aryana, J. T. Gaskins, J. Nag, D. A. Stewart, Z. Bai, S. Mukhopadhyay, J. C. Read, D. H. Olson, E. R. Hoglund, J. M. Howe, A. Giri, M. K. Grobis and P. E. Hopkins, Interface controlled thermal resistances of ultra-thin chalcogenide-based phase change memory devices, *Nat. Commun.* 2021, **12**, 774. DOI: 10.1038/s41467-020-20661-8

(29) H. K. Lyeo, D. G. Cahill, B. S. Lee, J. R. Abelson, M. H. Kwon, K. B. Kim, S. G. Bishop and B. k. Cheong, Thermal conductivity of phase-change material Ge2Sb2Te5, *Appl. Phys. Lett.* 2006, **89**, 151904. DOI: 10.1063/1.2359354

(30) S. Lee, K. Hippalgaonkar, F. Yang, J. Hong, C. Ko, J. Suh, K. Liu, K. Wang, J. J. Urban, X. Zhang, C. Dames, S. A. Hartnoll, O. Delaire and J. Wu, Anomalously low electronic thermal conductivity in metallic vanadium dioxide, *Science* 2017, **355**, 371–374. DOI: 10.1126/science.aag0410

(31) C. Liu, C. Wu, Y. Zhao, Z. Chen, T. L. Ren, Y. Chen and G. Zhang, Actively and reversibly controlling thermal conductivity in solid materials, *Phys. Rep.* 2024, **1058**, 1–32. DOI: 10.1016/j.physrep.2024.01.001

(32) P. Ben Abdallah and S. A. Biehs, Near-field thermal transistor, *Phys. Rev. Lett.* 2014, **112**, 044301. DOI: 10.1103/PhysRevLett.112.044301

(33) Y. Nishimura, X. He, T. Katase, T. Tadano, K. Ide, S. Kitani, K. Hanzawa, S. Ueda, H. Hiramatsu, H. Kawaji, H. Hosono and T. Kamiya,

Electronic and Lattice Thermal Conductivity Switching by 3D−2D Crystal Structure Transition in Nonequilibrium (Pb1−xSnx)Se, *Adv. Electron. Mater.* 2022, **8**, 2200024. DOI: 10.1002/aelm.202200024

(34) A. Jayaraman, V. Narayanamurti, E. Bucher and R. G. Maines, Continuous and Discontinuous Semiconductor-Metal Transition in Samarium Monochalcogenides Under Pressure, *Phys. Rev. Lett.* 1970, **25**, 1430–1433. DOI: 10.1103/PhysRevLett.25.1430

(35) A. Jayaraman, P. Dernier and L. D. Longinotti, Study of the valence transition in SmS induced by alloying, temperature, and pressure, *Phys. Rev. B* 1975, **11**, 2783–2794. DOI: 10.1103/PhysRevB.11.2783

(36) B. Batlogg, E. Kaldis, A. Schlegel and P. Wachter, Electronic structure of Sm monochalcogenides, *Phys. Rev. B* 1976, **14**, 5503–5514. DOI: 10.1103/PhysRevB.14.5503

(37) A. Sousanis, P. F. Smet and D. Poelman, Samarium Monosulfide (SmS): Reviewing Properties and Applications, *Materials (Basel)* 2017, **10**, 953. DOI: 10.3390/ma10080953

(38) K. Benbachir, J. Mazuer and J. P. Senateur, Low temperature thermal conductivity of pure and doped single crystals of semiconducting SmS, *Solid State Commun.* 1985, **54**, 965–968. DOI: 10.1016/0038-1098(85)90165-6

(39) B. H. Toby and R. B. Von Dreele, GSAS-II: the genesis of a modern open-source all purpose crystallography software package, *J. Appl. Crystallogr.* 2013, **46**, 544–549. DOI: 10.1107/s0021889813003531

(40) M. M. Sadeghi, Y. Huang, C. Lian, F. Giustino, E. Tutuc, A. H. MacDonald, T. Taniguchi, K. Watanabe and L. Shi, Tunable electron-flexural phonon interaction in graphene heterostructures, *Nature* 2023, **617**, 282–286. DOI: https://doi.org/10.1038/s41586-023-05879-y

(41) K. G. Subhadra and D. B. Sirdeshmukh, X-ray determination of the mean amplitudes of vibration and debye temperatures of some rare earth monochalcogenides, *Pramana* 1977, **9**, 223–227. DOI: 10.1007/bf02846201

(42) G. Güntherodt and R. Merlin. Raman scattering in rare-earth chalcogenides. In *Light Scattering in Solids IV*, Topics in Applied Physics, Vol. 54; 1984; pp 243–287.

(43) P. Wachter, Electronic structure, magnetic exchange, and electrical transport properties of the magnetic compounds EuS, GdS and GdP, *Phys. Rep.* 1978, **44**, 159–186. DOI: 10.1016/0370-1573(78)90001-7

(44) W. Beckenbaugh, J. Evers, G. Güntherodt, E. Kaldis and P. Wachter, Non-stoichiometric metals with strongly varying electron concentration: Gd-monochalcogenides and LaS, *J. Phys. Chem. Solids* 1975, **36**, 239–248. DOI: 10.1016/0022-3697(75)90016-5

(45) P. J. Robinson, J. Munarriz, M. E. Valentine, A. Granmoe, N. Drichko, J. R. Chamorro, P. F. Rosa, T. M. McQueen and A. N. Alexandrova, Dynamical Bonding Driving Mixed Valency in a Metal Boride, *Angew. Chem.* 2020, **132**, 11089–11095. DOI: 10.1002/ange.202000945

(46) M. Copel, M. A. Kuroda, M. S. Gordon, X. H. Liu, S. S. Mahajan, G. J. Martyna, N. Moumen, C. Armstrong, S. M. Rossnagel, T. M. Shaw, P. M. Solomon, T. N. Theis, J. J. Yurkas, Y. Zhu and D. M. Newns, Giant piezoresistive on/off ratios in rare-earth chalcogenide thin films enabling nanomechanical switching, *Nano Lett.* 2013, **13**, 4650–4653. DOI: 10.1021/nl401710f

(47) P. M. Solomon, B. A. Bryce, M. A. Kuroda, R. Keech, S. Shetty, T. M. Shaw, M. Copel, L. W. Hung, A. G. Schrott, C. Armstrong, M. S. Gordon, K. B. Reuter, T. N. Theis, W. Haensch, S. M. Rossnagel, H. Miyazoe, B. G. Elmegreen, X. H. Liu, S. Trolier-McKinstry, G. J. Martyna and D. M. Newns, Pathway to the piezoelectronic transduction logic device, *Nano Lett.* 2015, **15**, 2391–2395. DOI: 10.1021/nl5046796

Materials Horizons COMMUNICATION

View Article Online
DOI: 10.1039/D6MH00642F